EARTH SURFACE PROCESSES AND LANDFORMS
Earth Surf. Process. Landforms **37**, 680–691 (2012)
Published in 2012 by John Wiley and Sons, Ltd.
Published online 8 February 2012 in Wiley Online Library
(wileyonlinelibrary.com) DOI: 10.1002/esp.3206

Rock fall dynamics and deposition: an integrated analysis of the 2009 Ahwiyah Point rock fall, Yosemite National Park, USA

Valerie L. Zimmer,[1]* Brian D. Collins,[2] Greg M. Stock[3] and Nicholas Sitar[1]
[1] Department of Civil and Environmental Engineering, University of California, Berkeley, CA, USA
[2] US Geological Survey, Menlo Park, CA, USA
[3] National Park Service, Yosemite National Park, El Portal, CA, USA

Received 7 June 2011; Revised 5 December 2011; Accepted 19 December 2011

*Correspondence to: Valerie L. Zimmer, Department of Civil and Environmental Engineering, University of California, Berkeley, CA, 94720, USA. E-mail: vlzimmer@gmail.com

ESPL
Earth Surface Processes and Landforms

ABSTRACT: We analyzed a combination of airborne and terrestrial LiDAR, high-resolution photography, seismic, and acoustic data in order to gain insights into the initiation, dynamics, and talus deposition of a complex rock fall. A large (46 700 m^3) rock fall originated from near Ahwiyah Point in eastern Yosemite Valley and fell a total of 730 m to the valley floor on 28 March 2009. Analyses of remote sensing, seismic, and acoustic data were integrated to reconstruct the rock fall, which consisted of (1) the triggering of a 25 400 m^3 rock block in an area of intersecting and sometimes highly weathered joint planes, (2) the sliding and subsequent ballistic trajectory of the block from a steeply dipping ledge, (3) dislodging of additional rock from the cliff surface from beneath the rock fall source area, (4) a mid-cliff ledge impact that detached a volume of rock nearly equivalent in volume to the initial block, (5) sliding of the deteriorating rock mass down the remainder of the cliff, and (6) final impact at the base of the cliff that remobilized the existing talus downward and outward and produced an airblast that knocked down hundreds of trees. The depositional geomorphology indicates that the porosity of the fresh talus is significantly lower than that expected for typical blocky talus slopes, likely because the rock debris from this event was pulverized into smaller, more poorly sorted fragments and densified via dynamic compaction when compared to less energetic, fragmental-type rock falls. These results suggest that accumulation of individual rock-fall boulders tends to steepen talus slopes, whereas large, energetic rock falls tend to flatten them. Detachment and impact signals were recorded by seismic and acoustic instruments and highlight the potential use of this type of instrumentation for generalized rock fall monitoring, while LiDAR and photography data were able to quantify the cliff geometry, rock fall volume, source and impact locations, and geomorphological changes to the cliff and talus. Published in 2012. This article is a US Government work and is in the public domain in the USA.

KEYWORDS: rockfall; LiDAR; seismic; Yosemite Valley; talus

Introduction

Rock falls pose a significant hazard in steep, mountainous terrain such as that found in Yosemite National Park in California, USA. The same steep cliffs and scenic vistas that draw approximately four million visitors per year pose a rock fall hazard of 40 to 50 events each year, most of them small ($< 1000\ m^3$) (Wieczorek and Snyder, 2004; and subsequent unpublished observations). Large rock falls ($> 10\,000\ m^3$), which can sometimes pose greater hazard, are less frequent, typically occurring on decadal timescales (Wieczorek *et al.*, 1995; Guzzetti *et al.*, 2003). Understanding large rock falls is critical for assessing hazard, but can be challenging because these events are infrequent and sometimes difficult to document. Investigating the failure dynamics of these larger rock falls when they occur is therefore important for identifying potential outcomes from future events; new monitoring and remote sensing techniques can be especially helpful in constraining the dynamics of these events.

In many cases, large rock falls appear to be singular, instantaneous events involving the detachment and subsequent impact of previously intact rock masses. However, rock falls often consist of a series of events, including the initial failure of the rock mass, the breakup of falling rocks as they strike and ricochet from the cliff face, multiple large impacts of rock with the ground surface, energetic impacts on talus slopes, and the deceleration of the rocks as they roll and slide to a stop. Impacts along the cliff face may cause additional rock to break off and in some cases can result in pulverization of the rock mass if the impacts are sufficiently energetic. In addition, sliding and ballistic trajectories at different incident angles may affect the magnitude and eventual deposition characteristics of rock debris. This may lead to potentially unaccounted for consequences such as the generation of relatively finer debris compared to less energetic rock falls and more complex seismic signals when recorded by monitoring instrumentation. Therefore, the dynamics of rock falls may control key geomorphological characteristics including the porosity and shape of

the depositional talus slope, which are often used for identifying relative rock fall hazard (e.g. Wieczorek *et al.*, 1999).

In anticipation of future rock falls, airborne laser scanning data, i.e. LiDAR, was collected for Yosemite Valley in 2006 and the entire valley was documented with high-resolution photography in 2008 (Stock *et al.*, 2011). In early 2009, we installed a small seismic and acoustic instrument network in Yosemite Valley with the hope of capturing rock falls at close (< 1 km) range. This installation happened to be operational when the largest rock fall event in Yosemite in over 20 years occurred from Ahwiyah Point, yielding a unique seismic and acoustic record of this large and complex event. The seismic data constrain the timing of the rock fall detachment, impact, and airblast, provides information about polarity and source mechanics, and can be used to search for precursor seismic signals leading up to failure. Following the rock fall, we repeated LiDAR surveys and high-resolution photography to quantify geomorphic change and map the geologic structure in the vicinity of the source area. Thus, the 2009 Ahwiyah Point rock fall was uniquely well documented, allowing quantitative analysis of the event dynamics and resulting landscape changes to the cliff and underlying talus slopes.

The 2009 Ahwiyah Point Rock Fall

On 28 March 2009, a series of rock falls occurred in eastern Yosemite Valley, originating from near the summit of Ahwiyah Point, which is located about 800 m northeast of Half Dome (Figure 1). According to eyewitness reports from rock climbers located across the valley from Ahwiyah Point, the series began with a large rock fall during the night, followed by several hours of punctuated smaller rock falls, culminating in the largest event at 5:26 a.m. local Pacific Daylight Savings Time (PDT) [4:26 a.m. Pacific Standard Time (PST) and 12:26 p.m. Greenwich Mean Time (GMT)]. Smaller rock falls continued for more than one month afterward.

The largest rock fall consisted of failure of a block that detached, slid off a ramp, fell approximately 350 m down the northwest face of Ahwiyah Point and impacted a prominent ledge, dislodging additional material. The combined rock fall debris continued down the cliff an additional 300 m and struck the top of the talus slope beneath the cliff, generating an airblast that knocked down hundreds of trees. The southern portion of the Mirror Lake Loop Trail, a popular hiking route, was buried in rock debris for a distance of nearly 300 m. Because the event occurred early in the morning, there were no injuries or fatalities associated with the event.

The rock fall impact was detected widely on strong motion seismic networks as far away as 350 km, registering as a magnitude 2·4 earthquake. This is only the second rock fall in Yosemite National Park that was assigned a seismic event identification number in the California strong motion seismic network earthquake record (the first was the 1996 Happy Isles rock fall; Uhrhammer, 1996; Wieczorek *et al.*, 2000), a testament to the size and energy generated from this event.

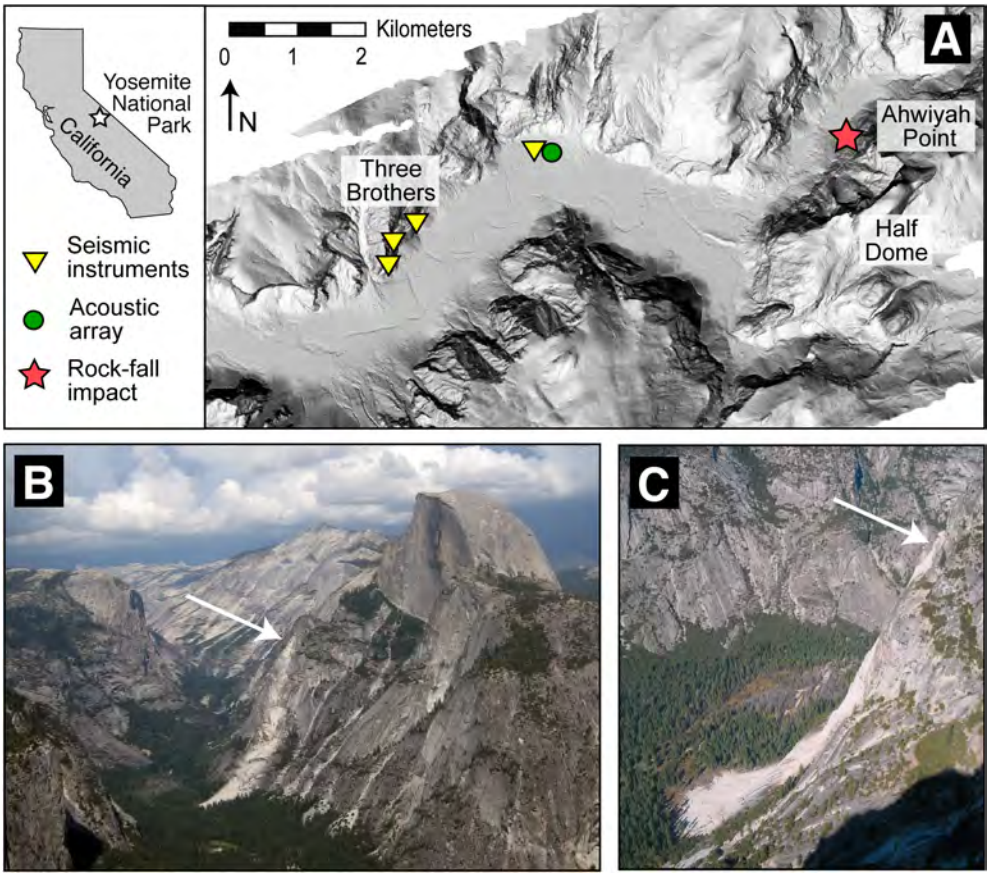

Figure 1. The Ahwiyah Point rock fall in eastern Yosemite Valley. (A) Map showing location of Ahwiyah Point rock fall and sites of seismic and acoustic instrumentation. Inset shows location of Yosemite National Park in California, USA and legend. (B) View of Ahwiyah Point and Half Dome (elevation 2693 m) from the west. The white streak in the center of the photograph is the runout path of the 28 March 2009 Ahwiyah Point rock fall. (C) View of the Ahwiyah Point rock fall runout zone from the northwest shoulder of Half Dome, showing the source area, travel path, and impact area on the floor of Tenaya Canyon (elevation 1247 m). Arrows mark the rock fall source area. This figure is available in colour online at wileyonlinelibrary.com/journal/espl

Geologic Setting and Rock Fall Triggering Mechanisms

Yosemite Valley is a classic U-shaped glacially-carved valley bounded by steep granitic rock walls that are nearly as tall as the valley is wide (approximately 1 km), and is the main attraction in Yosemite National Park. The steep cliffs are prone to rock falls that occur on average once a week, presenting a substantial rock fall hazard and corresponding risk to visitors, the majority of whom spend time in the narrow valley.

The history of rock falls, rock-fall triggering, and assessment of rock-fall hazards in Yosemite has been extensively studied (e.g. Wieczorek *et al.*, 1995, 1998, 1999, 2000, 2008; Wieczorek and Jäger, 1996; Wieczorek and Snyder, 1999, 2004; Wieczorek, 2002; Guzzetti *et al.*, 2003; Stock and Uhrhammer, 2010). Because Yosemite Valley experiences a high frequency of rock falls contained in a small geographic area, it represents an ideal laboratory for closely monitoring rock fall activity. Nearly 900 rock falls and other slope movement events (e.g. rockslides, debris slides, debris flows) have been documented during the period 1857–2011, with the majority of events occurring as rock falls in Yosemite Valley (Wieczorek and Snyder, 2004; and subsequent unpublished observations). These events resulted in 15 fatalities and numerous incidents where buildings, roads, and trails were damaged.

Whereas the cause of a rock fall is ultimately related to weathering, fracturing, and erosion of rock, the trigger that causes a metastable block of rock to become unstable and fall is often difficult to ascertain. Research has shown that approximately half of all documented failures in Yosemite are correlated with commonly recognized triggering mechanisms such as earthquakes, intense rainfall, snowmelt, or freeze–thaw conditions (Wieczorek and Jäger, 1996; Wieczorek and Snyder, 2004; and subsequent unpublished observations). The high proportion of rock falls that occur during or shortly thereafter these triggering conditions thereby suggests an association. Still, approximately half of all documented rock falls in Yosemite have no recognized trigger, nor were they part of a continuing series from a single source area. In the case of the Ahwiyah Point rock fall investigated here, we identify wet (snowmelt) and/or cold (freeze–thaw) conditions that occurred in late March 2009 as the most likely trigger(s). However, helicopter-based observations and analysis of close-range photographs taken after the rock fall suggests that portions of the rock mass were in a state of deterioration from long-term weathering, suggesting that the source area may have been in a metastable state and that progressive weathering may have played a contributory role in triggering the rock fall.

Seismic Monitoring of Rock Falls

Seismic studies pertaining specifically to rock falls are not common in the scientific literature, although cases of seismic monitoring efforts for landslides and rockslides are numerous (Spillman *et al.*, 2007; Roth and Blikra, 2009; Got *et al.*, 2010; Helmstetter and Garambois, 2010; Lacroix and Helmstetter, 2011). Seismic monitoring of rock falls can be viewed as a natural extension of these efforts and there has been some work on the subject of searching for triggers and precursors to failure (Amitrano *et al.*, 2005; Moore *et al.*, 2007). Precursory activity is sometimes observed as smaller rock falls or cracking noises in the days or hours leading up to a large failure but are often not reported until after a catastrophic event has occurred; such precursor activity has been noted for many rock falls in Yosemite Valley (Wieczorek and Snyder, 2004; and subsequent unpublished observations). These cases indicate that movement or fracture propagation prior to rock fall failure produces noise with sufficient energy to be audible and possibly seismically detectable.

Rock falls and rockslides have been detected in several cases by strong motion seismic networks that recorded impacts from these events (Uhrhammer, 1996; Wieczorek *et al.*, 2000; Deparis *et al.*, 2008; Dammeier *et al.*, 2011). Seismic stations as far as 200 km away recorded the 10 July 1996 Happy Isles rock fall in Yosemite Valley. This rock fall occurred with two main impacts 13·6 seconds apart, registering as two earthquakes of M1·5 and M2·1, respectively, and produced an airblast that knocked down more than 1000 trees (Morrissey *et al.*, 1999; Uhrhammer, 1996; Wieczorek *et al.*, 2000). Following the 1996 Happy Isles and the 1998–1999 Curry Village rock falls at Glacier Point, Myers *et al.* (2000) attempted to monitor rock falls there with seismic instruments. The results were inconclusive, however, as there were no notable rock falls during that time period and no other recorded signals could be definitively related to rock falls. From 2007 to 2009, we initiated further seismic and acoustic monitoring studies and captured the 2009 Ahwiyah Point rock fall, which happens to be the largest rock fall event in Yosemite Valley in more than 20 years.

Methods

High-resolution digital photography

High-resolution (gigapixel) photographs of the Ahwiyah Point area were acquired prior to the 28 March 2009 Ahwiyah Point rock fall as part of the Yosemite xRez project (http://www.xrez.com/case-studies/national-parks/yosemite-extreme-panoramic-imaging-project/), which photographed cliffs throughout Yosemite Valley (Stock *et al.*, 2011). Ahwiyah Point was photographed from three locations on the rim of Yosemite Valley and Tenaya Canyon. After the rock fall, we took photographs from the same vantage points in lighting conditions as similar as possible to the original photographs. These before-and-after photographs provide information and evidence for the pre- and post-rock fall cliff geometry, rock fall volumes, impact zones, and talus configuration.

LiDAR data collection and processing

We performed analyses of existing and new airborne LiDAR data and new terrestrial LiDAR data to obtain rock fall volume estimates and reconstruct failure surfaces for geomorphic and structural analyses of the event. Airborne LiDAR data were collected in 2006 before the Ahwiyah Point rock falls, and then again in 2010 following the rock falls, by the National Center for Airborne Laser Mapping (NCALM). Yosemite Valley was scanned from low-altitude aircraft (e.g. in 2010, a mean flying height of 700 m above ground level) using an Optech scanner; the resulting data has a typical raw-data point spacing of approximately 0·75 m. In the analyses presented herein, we used approximately 676 000 and 1 431 000 points from the overall 2006 and 2010 airborne datasets, respectively. We collected terrestrial LiDAR data in May 2009, approximately two months after the Ahwiyah Point rock fall, using a Riegl Z420i instrument from two scan positions located 1150 m from the rock fall source area on the north bank of Tenaya Creek. Although this vantage point provided high-resolution detail of the main rock fall area, including the roofs formed by the source area, we were not able to collect data in the lower rock

fall runout area due to excessive vegetation blocking our line-of-site. In total, we collected over 13 056 000 points from this data collection effort and used approximately 9 391 000 of these for surface modeling and geomorphic analysis. Typical raw-data point-spacing of the terrestrial LiDAR is approximately 20 cm, although at the farthest ranges, surfaces oriented oblique to the laser impulse reflection were not covered in as high resolution. However, even at these locations, we were able to reconstruct reasonable estimates of the post-failure geometry, which were later updated with data from the 2010 aerial LiDAR.

We processed LiDAR data using I-SiTE Studio software (Maptek, 2011). Due to a lack of sufficient survey control at our terrestrial LiDAR scanning position beneath the trees on the valley floor, we used surface registration algorithms to find the best fit (26 cm using a combination of 1296 similar points) between unchanged areas in the airborne and terrestrial LiDAR point and surface datasets. We confirmed the registration fit through detailed visual observation of cross-sections generated from each point cloud dataset. Given the point-spacing of the airborne data set (75 cm), this fit is acceptable for surface modeling and volumetric calculations at this scale.

Following a standard suite of filtering algorithms to remove vegetation and obtain a homogenously dense set of point clouds, we constructed spherical surface triangulation models (Maptek, 2011) specifically designed to model steep and overhanging terrain such as is found in Yosemite Valley. We discretized the rock fall area into five zones (Figure 2) consisting of the source area (Zone 1), an upper falling/sliding zone (Zone 2), an initial impact zone on the lower promontory (Zone 3), a lower falling/sliding zone (Zone 4), and a final impact/talus zone (Zone 5). Structural and distance measurements were computed using internal software scripts. We computed volumes based on three-dimensional comparisons between the constructed surfaces from the LiDAR data and averaged the results where appropriate (e.g. two volume estimates of the source area were performed, one each using the 2009 terrestrial data and the 2010 aerial data).

The rock fall remobilized a significant volume of existing talus on the valley floor upon final impact. To account for this, we identified and calculated both the overall and remobilized volumes of talus and subtracted the remobilized volume from the overall amount resulting in a net talus volume. We then calculated a new talus porosity by dividing the volume of talus voids (i.e. the net talus volume minus the total rock fall volume) by the net talus volume.

Seismic data collection and processing

We performed analysis of seismic data gathered from regional broadband seismic networks as well as a local Yosemite Valley network installed temporarily for the purpose of monitoring rock falls. Broadband data were acquired from the Northern California Earthquake Data Center (NCEDC), the Southern California Earthquake Data Center (SCEDC), and the California Department of Water Resources (WR). The contributing sources of the NCEDC data were from the Berkeley Seismological Laboratory, University of California, Berkeley (BDSN – BK), Northern California Seismic Network, US Geological Survey, Menlo Park (NCSN – NC), and the Seismological Laboratory, University of Nevada, Reno (UNR – NN). The contributing source for the SCEDC data was the Caltech Regional Seismic Network (CI).

At the time of the Ahwiyah Point rock fall, there were six local seismic stations in operation at four different sites within Yosemite: five on the Middle Brother formation 6·2 to 6·7 km away from the rock fall, and one on the floor of Yosemite Valley near Yosemite Village, located 4·4 km away from the source (Figure 1A). The instruments consisted of four 4·5 Hz geophones and two accelerometers with Reftek RT-130A/B dataloggers recording continuous data at either 500 or 1000 samples per second. We chose the instrument type and sampling rates based on limited data on rock fall and rock mass monitoring which indicated that this configuration would be adequate for rock fall detection (Amitrano *et al.*, 2005; Spillman *et al.*, 2007; Vilajosana *et al.*, 2008; Got *et al.*, 2010; Helmstetter and Garambois, 2010; Lacroix and Helmstetter, 2011). Seismic data were filtered in the 1–20 Hz and/or 2–8 Hz band for event detection and then rotated to radial and transverse components for polarity analysis and calculation of apparent velocity for P and S wave phases. We then filtered data in the 0·3–0·5 Hz band and rotated them to radial and transverse

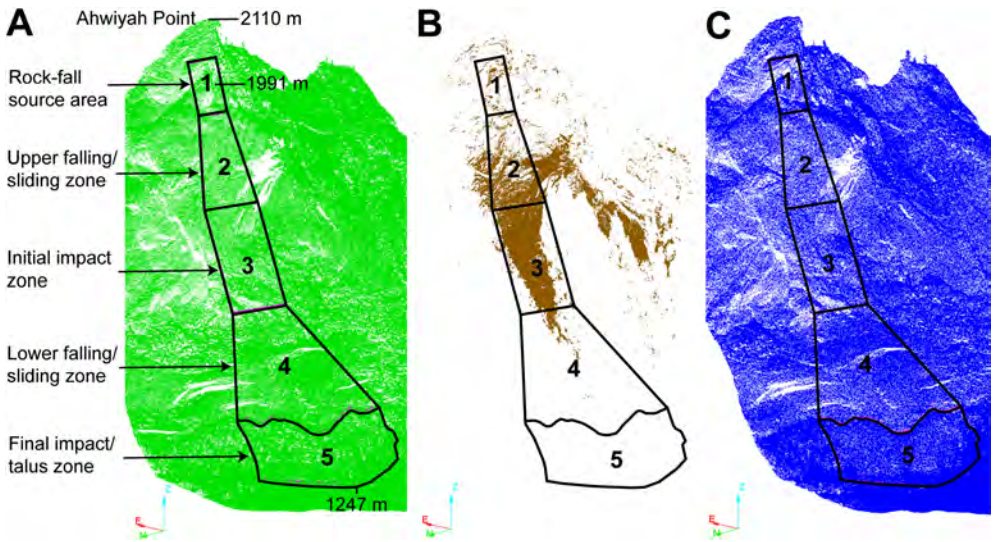

Figure 2. Point clouds from (A) airborne LiDAR collected before the 28 March 2009 Ahwiyah Point rock fall (2006), (B) terrestrial LiDAR collected after the rock fall (2009), and (C) airborne LiDAR collected after the rock fall (2010). Black polygons indicate the five zones investigated, as described in the text. Post-rock fall terrestrial LiDAR data was collected primarily to evaluate change in Zones 1–3, whereas post-rock fall airborne LiDAR data was collected primarily to evaluate change in Zones 4 and 5. To clearly illustrate the data, not all points are shown – in all cases, the point density used in analyses was significantly higher. This figure is available in colour online at wileyonlinelibrary.com/journal/espl

components for Rayleigh wave phase identification. We manipulated seismic data using the waveform suite in Matlab (Reyes and West, 2011).

Seismic data were used to constrain some of the physical parameters of the rock fall. In this case, differences in timing (t) of detachment, impact, and airblast events were used to constrain the sliding and freefall distance (d) using Equation 1.

$$d = \left(\frac{a^* t^2}{2}\right) + v_0 * t \quad (1)$$

where a is acceleration and v is velocity. The acceleration of rock sliding down a slope with inclination (β) can be related to the coefficient of friction (μ) of the rock mass by Equation 2 (Erismann and Abele, 2001).

$$a = g(\sin\beta - \mu\cos\beta) \quad (2)$$

where μ is equal to the tangent of the friction angle (θ), and g is the gravitational constant.

Acoustic data collection and processing

We installed three barometric infrasonic microphones in Yosemite Valley approximately 4·4 km west of Ahwiyah Point, but at the time of the rock fall only two were in operation. This type of microphone is primarily used to augment seismic networks very near to volcanoes (e.g. Johnson *et al.*, 2004) and records acoustic signals in the sub-audible range (below 20 Hz). Signals recorded by the infrasound microphones were processed by bandpass filtering between 0·1 and 10 Hz, picking the initial wave arrival, and back-calculating the acoustic velocity to confirm that the timing of the wave was appropriate to be associated with the rock fall. The waves were cross-correlated to give an accurate time-separation between the arrivals of the wavefront at each microphone. The azimuth of the incoming acoustic wavefront can be calculated with only a few meters separation of the microphones and normal global positioning system (GPS) precision in timing since acoustic waves travel relatively slowly. Technically, four microphones are required to establish an azimuth in a three-dimensional space, but if microphones are placed on flat ground and it is assumed that the acoustic signal is coming from the air (above), three microphones can suffice to locate an incoming signal. With only two microphones in operation at the time of the Ahwiyah Point rock fall, the incoming plane wave could only be isolated to a cone of possibilities. We then stacked the acoustic waveforms with the appropriate time-delay to enhance the signals originating in the direction of the rock fall. Waveform stacking effectively increases the signal-to-noise ratio, which helped to identify signals previously embedded in noise.

Results

Rock fall volumes, talus porosity and structural geometry

Our analyses of LiDAR data indicate that a total of 46 700 m^3 of intact rock mobilized during the Ahwiyah Point rock falls and covered an area on the valley floor measuring 64 000 m^2 to a depth of up to 8 m. The vast majority of the rock mobilized during the event at 5:26 a.m. PDT on 28 March 2009. We estimate an approximate level of uncertainty of ± 1–5% in the overall volume measurement. The total volume consists of 25 400 m^3 from the rock-fall source area (Figure 3), 2000 m^3 from intermediate blocks dislodged as the rock mass traveled downwards along the upper cliff face, and 19 300 m^3 from the mid-cliff impact of the rock fall on the lower promontory (Figure 4). A minor additional amount of rock (estimated to be less than 1000 m^3) was detached below this point and prior to final impact. Upon final impact at the base of the cliff, the rock fall remobilized an additional 7000 m^3 of existing accumulated talus, pushing the upper portion of the talus slope downward and outward (Figure 5). The average talus slope angle was reduced from 31° to 29°, the height of the talus at the apex was lowered by up to 13 m, and the toe was extended by 48 m horizontally for a 50 m distance parallel to the base. The porosity of the new talus deposit is estimated to be between 7 and 16%, with a best estimate of 14%. The

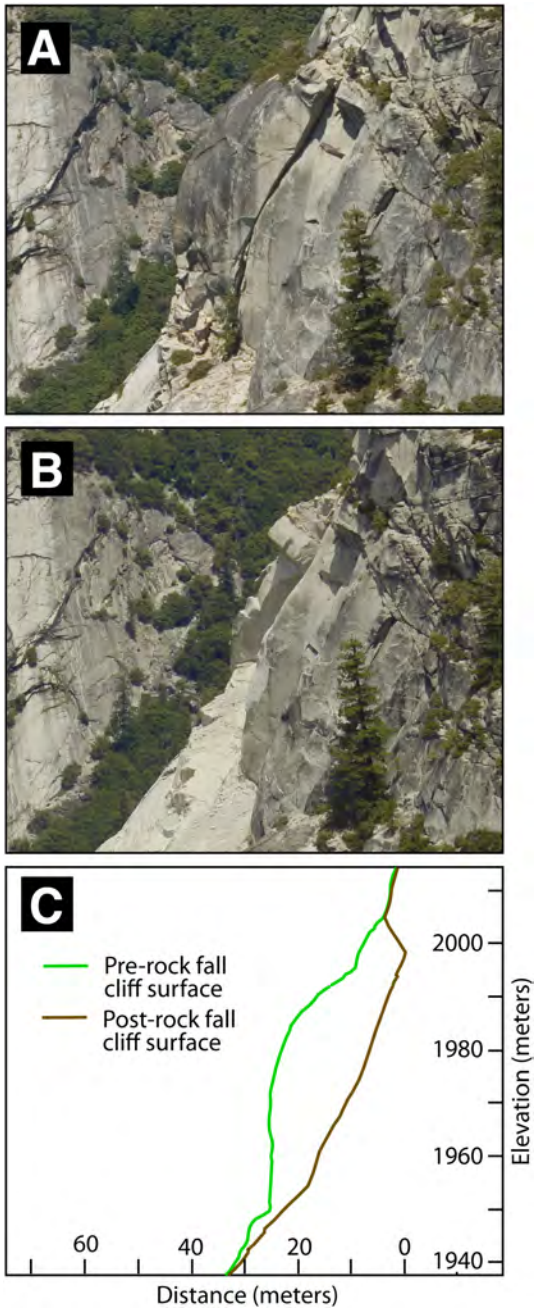

Figure 3. High-resolution digital photographs of the rock-fall source area (A) before and (B) after the 28 March 2009 Ahwiyah Point rock fall, showing the size and position of the failed block, and (C) cross-section showing prominent roof structure at top of block. This figure is available in colour online at wileyonlinelibrary.com/journal/espl

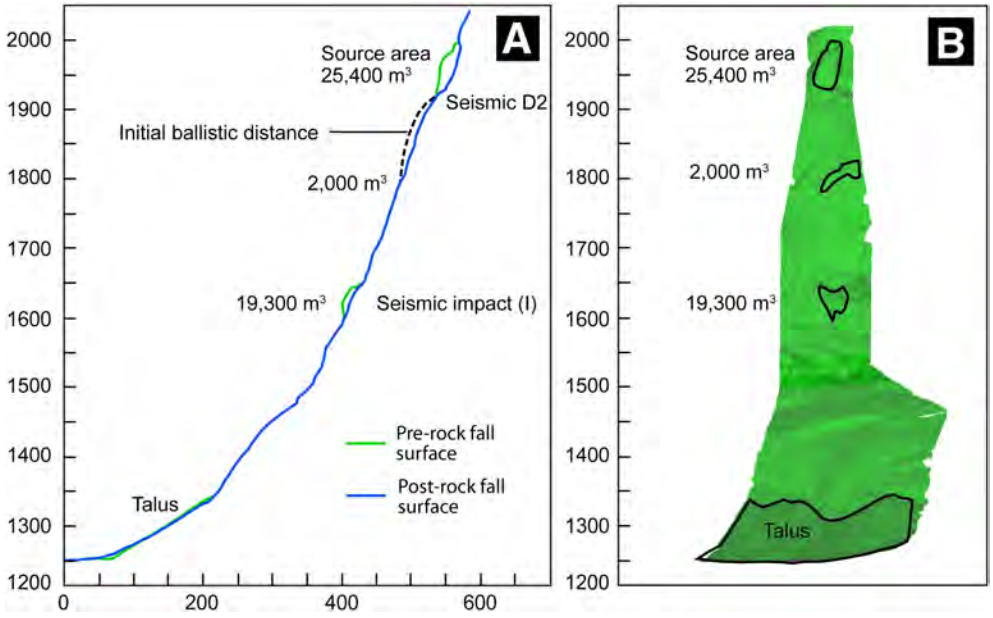

Figure 4. Views of the Ahwiyah Point cliff in (A) cross-section and (B) frontal view. Elevations and volumes of the source area, the ballistic trajectory and location of material knocked out enroute, the prominent midcliff ledge where a large impact knocked out a significant amount of material, and the talus slope are shown. This figure is available in colour online at wileyonlinelibrary.com/journal/espl

variability is indicative of the difficulties with filtering LiDAR data associated with vegetation on the rough surface that formed the talus slope prior to the rock fall, and in separating the contributions between new and remobilized talus.

Cross-sections generated through the pre- and post-rock fall surfaces show that the source block consisted of an 80 m long, 50 m wide, 26 m thick block, measured at its maximum dimensions (Figure 3). The normal to the cliff face is oriented at an azimuth of approximately 285° (northwest) in the vicinity of the rock fall. Analysis of the point and surface data show that failure occurred along the intersection of four prominent intersecting planes (joints) consisting of an approximately 67° inclined, northwest-dipping surface (approximate dip/dip direction: 67°/322°), a 67° inclined, west-dipping surface (approximate dip/dip direction: 67°/272°), a 90° inclined, west-dipping surface (approximate dip/dip direction: 90°/236°) and a 46° inclined, west dipping surface (approximate dip/dip direction: 46°/262°) which formed the bottom sliding surface of the rock fall. Although we did not perform a full structural analysis of the area, comparison of high-resolution photographs and the LiDAR data reveals that each of the planes within the rock fall source area appear to be part of prominent joint sets in the immediate vicinity of the rock fall and that they approximately correspond respectively to the J9, J6, J7, and J5 joint sets recognized elsewhere in Yosemite Valley (Wieczorek *et al.*, 2008). The source block was further bounded by several east dipping roofs inclined at between 51° and 59° (average dip/dip direction: 56°/097°). We identified planes (roofs) with similar orientations adjacent to the source area, indicating that this joint set is also likely pervasive throughout the area.

Analysis of the mid-cliff impact zone indicates that a wedge formed by two intersecting planes (joints) was dislodged by the impact of rock debris from above. The wedge is formed by the intersection of a 59° inclined, northwest-dipping surface (approximate dip/dip direction: 59°/319°) and a 58° inclined, southwest-dipping surface (approximate dip/dip direction: 58°/224°), corresponding roughly to the previously identified J9 and J6 joint sets (Wieczorek *et al.*, 2008).

Rock fall progression events, phases, and, polarization from seismic monitoring

The 28 March 2009 Ahwiyah Point rock fall produced distinct ground motion records on 107 seismic stations ranging from 4·4 km to 353 km from the point of impact (Figure 6). The event registered as a magnitude 2·4 earthquake with an event time of 12:26:04.53 GMT. Close examination of the seismic records reveals that there are three distinguishable events associated with the rock fall. The mid-cliff ledge impact (Figure 4, at 1644 m elevation) is the largest, most distinct, and most easily identified part of the signal (P_I, Figures 6 and 7). Immediately preceding the impact (I) are two distinct smaller events, most likely relating to the detachment (P_{D1} at 9.6 ± 0.3 seconds) and initial movement (P_{D2} at 7.3 ± 0.3 seconds) of the rock mass prior to impacts on the cliff. The separation in detachment and impact signals can be clearly seen in a spectrogram (Figure 8), which shows an increase in overall energy and higher frequencies with each subsequent event as the rock fall progresses, before tapering off. After the mid-cliff impact, the seismic record remains noisy with rock impacts and multi-path arrivals of impact events. As a result, additional individual impacts and the airblast are not discernable from the seismic record.

All three of the distinguishable seismic events associated with the Ahwiyah Point rock fall are incoming compression (P) waves (P_{D1}, P_{D2}, P_I), as evidenced by their consistent separation in time with increasing distance, i.e. they all have the same slope in Figure 6. The slope of each line represents the average seismic velocity as the waves move out from the sources, and is called the moveout velocity. The P-wave moveout velocity is 5·9 km/s (Figure 6), a value consistent with near-surface velocity in granitic rock. The polarity of the impact P-wave is positive (compressive) in all directions. Of the four broadband triaxial stations within 100 km of Yosemite Valley, only two show an emergent shear (S) wave as well as a Rayleigh wave (Figure 7) associated with the impact event (S_I, Lr_I). There is no clear identification of S-waves at the other two broadband triaxial stations, nor at any of the six local seismic stations,

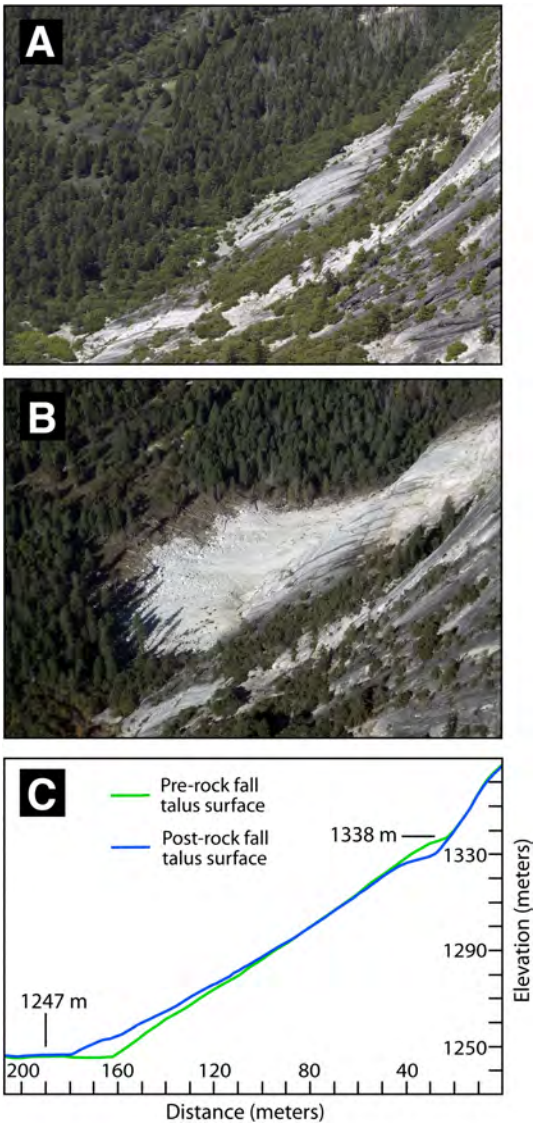

Figure 5. Images of the talus deposition zone (A) before and (B) after the rock fall with the airblast area visible beyond the edge of new talus. (C) Pre- and post-rock fall talus surface cross-sections show addition of new talus and remobilization of old talus resulting in a decrease in overall slope angle of ~2°. The talus apex was lowered up to 13 m and the toe pushed outward up to 53 m. The new talus deposit is composed chiefly of fine debris with only a few large boulders of mean diameter greater than 2 m. This figure is available in colour online at wileyonlinelibrary.com/journal/espl

although there does appear to be a second weak arrival with a moveout velocity of 3·4 km/s from the impact event, which is consistent with expected S-wave velocity (Figure 6, S_I). All 25 stations within 100 km, including broadband uniaxial stations, show a strong Rayleigh wave arrival (Lr_I) with a moveout velocity of 2·7 km/s from the impact event. As opposed to earthquakes, which emit distinct S-waves in addition to P-waves and Rayleigh waves, rock fall impacts emit mainly just strong P-waves and Rayleigh waves.

We examined the azimuth of the incoming seismic wave using two geophone stations in two different locations. The time difference in arrival at these stations and the relative first motion magnitudes of the three components indicates that seismic waves originating from the Ahwiyah Point rock fall were traveling along the face of the cliff and not directly on azimuth from the rock fall source. This is because the floor of Yosemite Valley consists of up to 600 m of sediment fill, resulting from Pleistocene glacial erosion and subsequent infilling (Gutenberg *et al.*, 1956) and has relatively slow seismic velocities when compared to the granitic bedrock cliffs. The velocity contrast means that much of the seismic energy traveling through the valley is reflected back into the basin rather than transmitted to the cliffs where the instruments were installed (Lay and Wallace, 1995), that seismic attenuation over the same distance is greater in the valley, and that waves traveling along the cliffs may have arrived earlier at the seismic stations than those traveling a shorter distance through the slower sediments. We could not calculate the exact azimuth using a third station because the geophone at the third location was malfunctioning and the signal-to-noise ratio of the two accelerometers was too low to accurately correlate individual arrivals with the geophones.

Infrasound acoustic signals

The Ahwiyah Point rock fall was heard as a rumbling sound by witnesses in nearby Yosemite Village and recorded by infrasound microphones (Figure 9). The back-calculated acoustic velocity from impact time (I) to signal onset is 325 m/s (± 17 m/s). This is consistent with a calculated acoustic velocity of ~333 m/s (Halliday *et al.*, 1993) at 3 °C (the air temperature at the time of the event). Cross-correlation of the two microphone waveforms pins the time delay at 0·042 seconds, which allows the azimuth of the incoming wavefront to be calculated and the waveforms to be stacked. The cone of incoming azimuths to the acoustic source is 239° to 315°, while the known azimuth from the rock fall is 263°, further confirming that the source of the acoustic signal is the Ahwiyah Point rock fall. The stacked waveform shows a signal arriving before the impact that coincides in timing with the seismic D2 event, seven seconds prior to impact, however, there is no acoustic signal corresponding to the seismic D1 event. Our interpretations indicate that the seismic D1 signal is the initial detachment (and low velocity sliding) of the source block, and that the D2 signal relates to the block leaving the ledge located immediately below the source. Because of the sensitivity band of the instrument (infrasound, i.e. sensitive to high-velocity movement of air in front of a large block) and the nature of a signal likely to be emitted from an initial detachment [i.e. a faint, high frequency (audible) cracking sound], the D1 signal should not have been picked up by this instrumentation.

Finally, at the end of the infrasound acoustic record, lowpass filtering at 0·5 Hz shows a strong low frequency acoustic wave arriving 3·3 seconds after the mid-cliff impact which is likely related to the airblast that caused the destruction of trees beyond the talus slope. The higher frequency impact and lower frequency airblast are clearly differentiated on a time-frequency spectral plot (Figure 8B).

Rock-fall trajectory and airblast analysis

The dynamics associated with the Ahwiyah Point rock fall as it progressed down the slope can be constrained using a combination of the seismic and LiDAR data, which pinpoint the locations of the source and impact areas and thus the acceleration and velocity profile. The LiDAR-calculated mid-cliff impact distance from the bottom of the block to the center of the impact is approximately 300 m, but there is also material (2000 m^3) knocked out *en route* approximately 120 m below the source area such that a trajectory to this location must also be investigated. Using the two

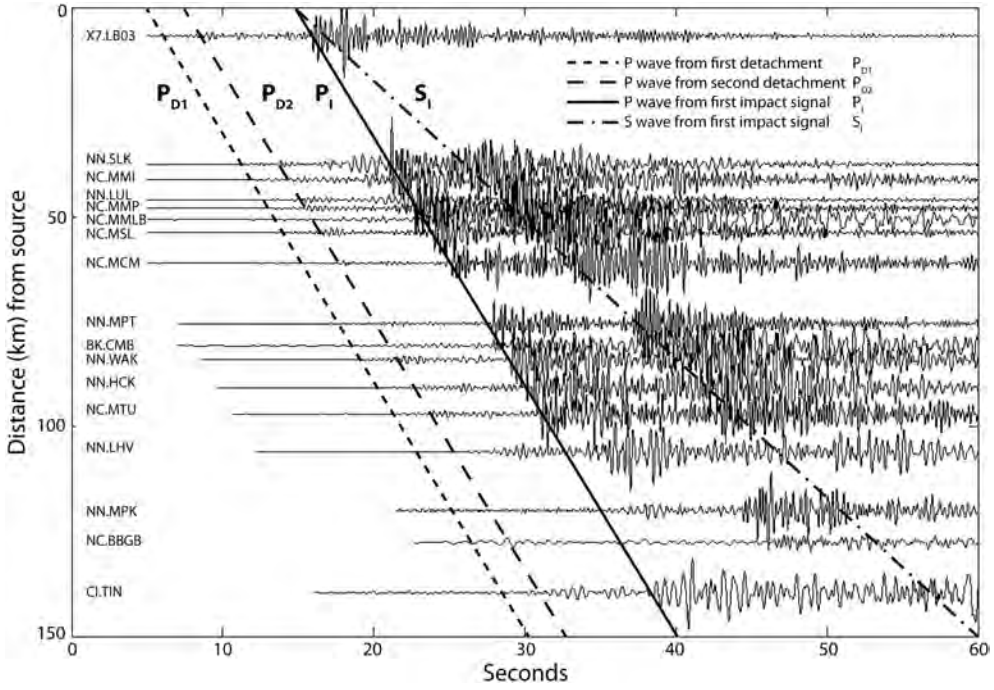

Figure 6. Recorded seismic signals at stations located from zero to 150 km from the rock fall. Lines are drawn to represent the arrivals of different seismic events (detachment, D or impact, I) and phases (P or S waves) from the same event. P waves are easy to distinguish, but the S wave arrival is more subtle and is not evident at all stations. The P wave moveout velocity (e.g. the line slope representing seismic apparent velocity) is 5·9 km/s, and the S wave moveout velocity is 3·4 km/s; these values are consistent with near-surface velocities in granitic rock.

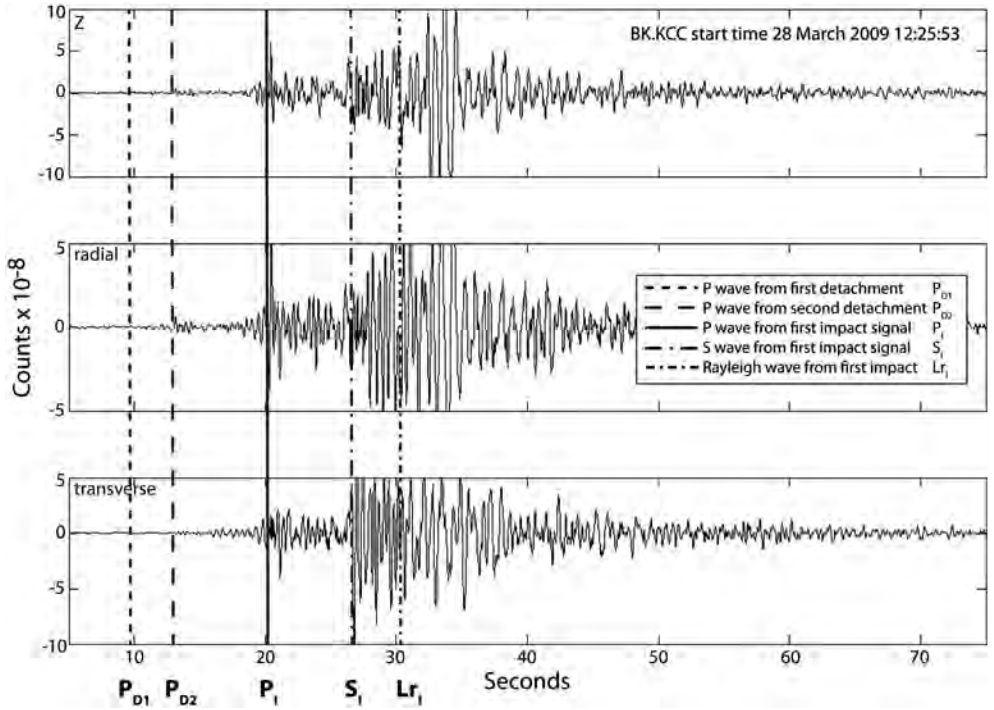

Figure 7. Broadband station KCC with three components: Z, radial, and transverse to the rock fall. All data is filtered 1–20 Hz. Lines are drawn to represent the arrivals of different seismic events (detachment or impact) and/or phases (compressional, P; shear, S; or Rayleigh waves, Lr) from the same event.

distinct detachment-related signals at 9·6 seconds (D1) and 7·3 seconds (D2) prior to the main impact (I), we can back-calculate the impact distances for both ballistic and sliding trajectories.

The block that detached from the source area was tall relative to its thickness, suggesting two possible modes of rock fall initiation: toppling and sliding. The block was bounded by three steeply dipping fracture surfaces, and rested on a 17 to 27 m wide ledge with downslope dip of 46°. Assuming a static friction angle for unpolished granite of between 42° and 51° (Goodman, 1989; Lajtai and Gadi, 1989) and that joint cohesion was minimal dictates that the detached block was, at best, metastable with respect to sliding. However, the fractures bounding the back of the failed rock mass and which formed the detachment surface are inclined at 67° and 90° obliquely to and away from the cliff face, and thus, the center of mass was well-within the bottom footprint of the block (Figure 3C), providing resistance to overturning moments. This, along with the steeply dipping ledge, suggests that the mode of initial failure was sliding, not toppling.

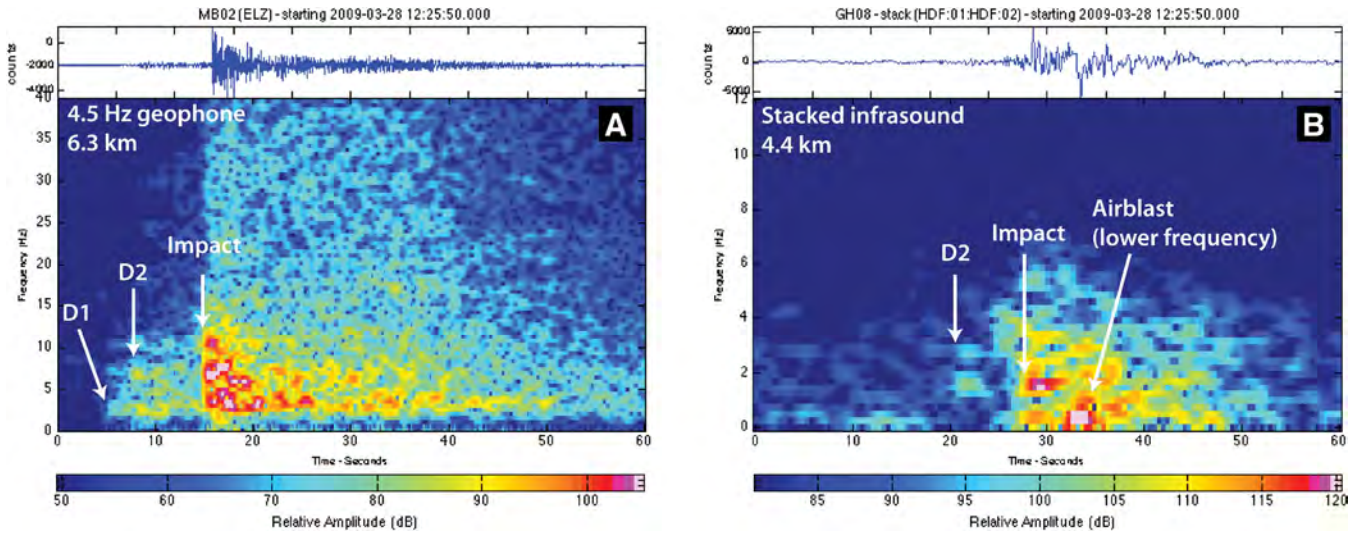

Figure 8. Spectrograms showing (A) geophone Z component and (B) stacked infrasound. The *X* axis represents time from zero to 60 seconds, and the *Y* axis represents frequency (in hertz) of incoming seismic waves. Red-yellow color indicates strong seismic response at that particular frequency and time, whereas blue colors indicate weak to no seismic response (e.g. random noise) at that frequency and time. This figure is available in colour online at wileyonlinelibrary.com/journal/espl

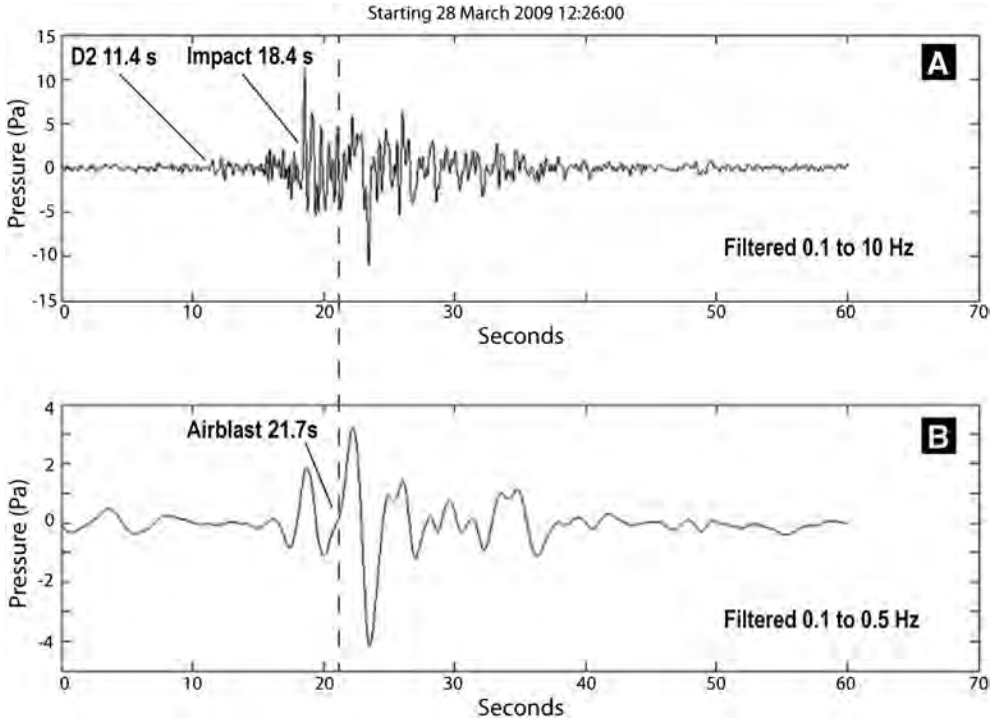

Figure 9. Stacked infrasound acoustic signal showing events associated with the Ahwiyah Point rock fall filtered from (A) 0·1 to 10 Hz and (B) 0·1 to 0·5 Hz.

The timing of the seismic signals can be used to verify the failure mode. A sliding block would travel obliquely to the cliff face in the ledge dip direction whereas other modes, such as toppling, might instead fall directly. The impact distance for a direct fall can therefore be calculated with error bounds reflecting the uncertainty in timing and model acceleration. The calculated direct fall impact distance assuming a toppling mode is 420 ± 60 m starting at time D1 and 240 ± 40 m starting at time D2. Because the fall distance from the bottom of the source area to the center of the impact zone is 300 m (i.e. not corresponding to either toppling scenario), the timing of D1 and D2 supports a hypothesis of initial sliding failure, rather than toppling.

We hypothesize that the block detached from its previous metastable configuration at time D1 and slid obliquely along on the dipping ledge until reaching the edge at time D2, at which point it launched ballistically for a short period of time (Figure 4). This is supported by a relatively steep launch velocity vector of 46° and steepening of the cliff to greater than 70° below the ledge. Following launch, the trajectory was controlled by the launch velocity and its vector, which is a function of the dip and dip direction of the ledge, the slide distance, and the friction angle. Modeling of a range of initial parameters (e.g. friction and sliding distance) reveals that the trajectory is highly sensitive to small changes in the initial parameters. LiDAR data provide the exact orientation and dimensions of the sliding surface (dip of 46°, dip direction of 262°, cliff face normal of 285°, and ledge dimensions of 17 to 27 m wide). Dynamic friction angle was estimated to be very low based on trajectory analysis from the 1996 Happy Isles rock fall in

Yosemite Valley, which slid down a 47° dipping ledge, went ballistic, and barely cleared a ledge *en route* to the ground, a scenario that is only possible with extremely low friction sliding (Wieczorek *et al.*, 2000). Therefore, we bound the sliding distance from 17 to 27 m, and the friction angle from 0° to 15°.

Using the minimum sliding distance of 17 m, we calculate that the block slides for $2{\cdot}4 \pm 0{\cdot}2$ seconds and falls ballistically 123 ± 7 m before contacting the cliff face. Using the maximum sliding distance of 27 m, we calculate that the block slides for $3{\cdot}0 \pm 0{\cdot}2$ seconds and falls ballistically 177 ± 10 m before contact. The results from the 17 m sliding scenario are a better match to both the distance to the material knocked off *en route* (120 m), as well as the time difference between initiation at D1 and launching at D2 (2·3 seconds).

Following the initial ballistic trajectory, the rock fall debris continued to fall down the steep (~70°) cliff face before impacting the prominent ledge 300 m below the bottom of source area and dislodging a wedge-shaped mass of rock (19 300 m^3) nearly equivalent in volume to the initial source block (25 400 m^3). This high energy impact is the source of the primary seismic signal, and results from the high velocity of the falling block (73 ± 5 m/s) and the change in slope from approximately 70° to approximately 35°.

Following the mid-cliff impact, the combined rock fall debris, now almost double in size compared to the initial rock fall volume and quickly disintegrating into finer fragments, continued down the lower angle (~55°) cliff face before impacting the talus slope. Upon impact, an airblast was produced that knocked over trees up to 50 m beyond the talus edge. The lower frequency infrasound acoustic wave arriving 3·3 seconds after the mid-cliff impact is likely related to the airblast. To verify this, we calculated the fall height using Equation 1, the timing of the airblast (3·3 seconds after impact), the mid-cliff impact velocity (73 ± 5 m/s), and an estimated vertical acceleration of $6{\cdot}6 +/- 0{\cdot}3$ m/s^2. The fall height below the mid-cliff impact is calculated to be between 260 m and 300 m (approximately 590 to 630 m below the rock fall source area) and is consistent with the actual dimensions of the rock fall and cliff geometry, verifying that the low frequency acoustic signal originated at the talus slope impact zone.

Discussion

Quantitative analysis of large complex rock falls improves understanding of the initiation mechanics and trajectory dynamics of rock falls that might pose a significant hazard. Using LiDAR and seismic monitoring contributes substantially to this type of analysis, and improves rock fall detection capabilities.

Structural mapping of the source and initial impact areas revealed that the detachment surfaces were part of regular joint patterns in their immediate vicinity. This observation suggests that mapping discontinuity planes throughout potentially hazardous cliff areas may inform on potentially unstable blocks, thereby contributing considerable information with regards to future rock fall volume possible (e.g. Jaboyedoff *et al.*, 2010). Whereas block theory has been well developed for many applications related to rock mechanics (e.g. Goodman and Shi, 1985), its use in LiDAR-based rock fall hazard studies is in its infancy in many regards and has much potential.

Analyses of repeat aerial LiDAR scans show that the rock fall was sufficiently energetic to remobilize approximately 7000 m^3 of previously accumulated talus in the upper part of the talus deposit; this volume was moved downward and outward, reducing the height of the talus apex along almost its entire length by up to 13 m and extending over 50 m of the toe of the talus slope by 48 m horizontally (Figure 5C). This movement changed the average talus slope angle from 31° prior to the rock fall to 29° after the rock fall. This result suggests that the cumulative debris from smaller, fragmental-type rock falls tends to accumulate near the tops of talus deposits, steepening the talus slope angle, whereas large energetic rock falls such as the Ahwiyah Point rock fall tend to push existing talus deposits downward and outward, flattening the talus slope angle.

Volumetric comparison of the source block with the fresh talus deposit allows for calculation of talus porosity (volume bulking). Our calculated porosity of ~14% is lower than what would be expected for blocky talus slopes (~30%; Sass and Wollny, 2001; Moore *et al.*, 2009). Most blocky talus slopes consist of individual boulders, likely derived from numerous relatively small rock falls, that experience gravity sorting (e.g. Evans and Hungr, 1993, and references cited therein). In contrast, the debris from the Ahwiyah Point rock fall consisted of considerable pulverized rock dust and smaller, more poorly sorted fragments than other talus slopes, which would result in a lower than average talus porosity. In addition, the high energy of this rock fall probably also dynamically compacted some of the existing talus. Debris from large, energetic rock falls may often become pulverized and densified due to disintegration of rock masses impacting mid-cliff ledges and the talus slope. This suggests that field investigations of talus porosity and/or talus slope angle may help identify other large, pre-historic rock falls and identify cliffs that are more susceptible to these types of rock falls.

Our analysis of seismic data shows that it is possible to identify rock fall impacts in the seismic record based on phase and polarity analysis, and furthermore, that distinct detachment and impact events can be traced to the physical trajectory of the rock fall. It follows that seismic monitoring may be able to identify progressive failure in the form of detachments that are unaccompanied by a total rock fall failure. Seismic and/or acoustic monitoring has potential to identify precursory cracking or smaller rock falls if the instruments are positioned sufficiently close to rock fall source areas. In the case of the Ahwiyah Point rock fall, no precursors or small rock falls were detected by the local seismic network, although through experience we have learned that smaller rock falls are usually not detectable at distances greater than 1 km. Furthermore, Rayleigh waves from the Ahwiyah Point rock fall arrived in frequencies well below the low sensitivity range of the geophone (i.e. the geophone corner) and are thus dampened by the instrument response (Figure 8A). This suggests that Rayleigh waves from smaller rock falls may be detectable with lower frequency geophones at greater distances. Audible cracking noises have been reported prior to large rock falls in Yosemite Valley (Wieczorek and Snyder, 2004; and subsequent unpublished observations), but the infrasound microphones did not record any unusual sounds prior to the Ahwiyah Point rock fall. However, the microphones we used are not highly sensitive to higher frequencies, nor are the sampling rates sufficiently high to detect cracking sounds. The infrasound microphones did, however, record the sliding of the source block off the ramp, the mid-cliff impact, and the final talus slope impact and airblast. The infrasound microphones were also able to constrain the range of azimuths for the incoming seismic waves, although with only two microphones in operation, it was not possible to pinpoint a single azimuth.

Finally, the success of the phase and polarity analysis for the impact event demonstrates that seismic sensors may be able to help identify the mechanism of failure for the detachment event if a there is a network of stations at different azimuths sufficiently close to the event. The question as to whether (and when) rock falls fail as a stress-induced burst, as crack propagation and shearing, or simple loss of fracture cohesion and frictional resistance to sliding could dramatically improve future hazard analyses in mountainous terrain.

Conclusions

Rock falls pose a significant hazard in mountainous terrain and can be better understood through quantitative analysis of large rock falls, particularly those with complex dynamics. The 28 March 2009 Ahwiyah Point rock fall was uniquely well-documented using a combination of LiDAR data, high resolution photography, seismic, and acoustic data.

Analysis of the LiDAR data accurately determined the volume and dimensions of the source block (25 400 m^3 with longest dimensions of 80 m long, 50 m wide, and 26 m thick), the orientation of the fractures bounding the block, the size (17–27 m) and dip (46°) of the ramp along which the block slid, the vertical ballistic distance (120 m), the mid-cliff impact distance (350 m from the center of the block), and the volume of material dislodged *en route* (2000 m^3) and from the mid-cliff impact (19 300 m^3). Photographic inspection shows deteriorating granite in the vicinity of the source area, suggesting that the bounding fractures might have been slowly losing strength due to weathering. However, given the timing of the event during late winter and the occurrence of snowmelt conditions immediately prior to the event, we suggest that snowmelt and/or freeze–thaw are the most likely triggering mechanisms for this rock fall.

Seismic stations as far as 350 km away detected this rock fall. Local (Yosemite Valley) seismic instruments recorded two distinct detachment signals and a large impact signal, which were well-matched to the sliding distance and impact location. The P-wave polarity of the impact was compressive, as would be expected from a surface impact event, and the relative strengths of the P, S, and Rayleigh wave phases is consistent with what might be expected from rock falls, suggesting that polarity and phase analysis can be used to identify other rock falls in the seismic record. Infrasound sensors recorded the second detachment signal associated with the initiation of the ballistic phase, as well as the impact and an airblast pulse that could be traced to the talus slope.

Trajectory analyses using the LiDAR and seismic data suggest that the rock fall started when the source block detached, slid down a steeply dipping ledge with very little friction, and launched into a short ballistic trajectory before contacting the wall and dislodging a relatively small amount of debris. The rock mass then continued to fall until impacting a prominent ledge with such force that a volume of additional rock nearly equivalent to the initial source block was dislodged from the cliff face as a wedge failure.

The force of the final impact on the talus slope was great enough to remobilize 7000 m^3 of pre-existing talus at the base of the cliff and produce an airblast, which knocked over hundreds of trees in a zone up to 50 m beyond the edge of the talus slope. The remobilized talus moved downward and outward, changing the average talus slope angle from 31° to 29°. This suggests that talus slope angles can preserve information on the size and dynamics of pre-historic rock falls. Volumetric comparison of the source block and the fresh talus deposit yields a talus porosity of 14%, a value lower than might be expected for blocky talus. This may result from a relatively high proportion of pulverized rock with consequently fewer air voids that was distributed over the entire talus slope.

Our results demonstrate that the combination of seismic, acoustic, LiDAR and high resolution photography data we obtained for the Ahwiyah Point rock fall can be used to document nearly all important aspects of this rock fall, including the structural and geomorphic conditions that led to failure, the precise timing and trajectory of the rock fall, the sequence of impacts and resulting volume changes, and the evolution of the talus slope due to the high energy impact. These tools offer valuable insights into the dynamics, geomorphology and associated hazards of large, complex rock falls in mountainous terrain.

Acknowledgments—This research was supported by the National Science Foundation (NSF) SGER Grant # 0840580 to N. Sitar and by the US Geological Survey Landslide Hazard Program to B. Collins. Seismic instruments were provided by the Defense Threat Reduction Agency and by the PASSCAL Instrument Center at New Mexico Tech, of the Incorporated Research Institutions for Seismology (IRIS). The facilities of the IRIS Consortium are supported by the National Science Foundation under Cooperative Agreement EAR-0552316 and by the Department of Energy National Nuclear Security Administration. Acoustic microphones were loaned by the InfraVolc Research Group at New Mexico Tech. Airborne LiDAR data collected in 2010 were provided through a National Center for Airborne Laser Mapping (NCALM) graduate student Seed project grant.

References

Amitrano D, Grasso, JR, Senfaute G. 2005. Seismic precursory patterns before a cliff collapse and critical point phenomena. *Geophysical Research Letters* **32**: L08314.

Dammeier F, Moore JR, Haslinger F, Loew S. 2011. Characterization of alpine rockslides using statistical analysis of seismic signals. *Journal of Geophysical Research* **116**: F04024. DOI. 10.1029/2011JF002037

Deparis J, Jongmans D, Cotton F, Baillet L, Thouvenot F, Hantz D. 2008. Analysis of rock-fall and rock-fall avalanche seismograms in the French Alps. *Bulletin of the Seismological Society of America* **98**(2): 1781–1796.

Erismann TH, Abele G. 2001. *Dynamics of Rockslides and Rockfalls*. Springer-Verlag: New York.

Evans SG, Hungr O. 1993. The assessment of rockfall hazard at the base of talus slopes. *Canadian Geotechnical Journal* **30**: 620–636.

Goodman RE. 1989. *Introduction to Rock Mechanics*. John Wiley & Sons: New York.

Goodman RE, Shi G-H. 1985. *Block Theory and its Application to Rock Engineering*. Prentice-Hall: Englewood Cliffs, NJ; 338 pp.

Got JL, Mourot P, Grangeon J. 2010. Pre-failure behaviour of an unstable limestone cliff from displacement and seismic data. *Natural Hazards and Earth System Sciences* **10**: 819–829.

Gutenberg B, Buwalda JP, Sharp RP. 1956. Seismic explorations on the floor of Yosemite Valley, California. *Geological Society of America Bulletin* **67**: 1051–1078.

Guzzetti F, Reichenbach P, Wieczorek GF. 2003. Rockfall hazard and risk assessment in the Yosemite Valley, California, USA; monitoring, modeling, and mapping of mass movements. *Natural Hazards and Earth System Sciences* **3**: 491–503.

Halliday D, Resnick R, Walker J. 1993. *Fundamentals of Physics*. John Wiley & Sons: New York.

Helmstetter A, Garambois S. 2010. Seismic monitoring of Séchilienne rockslide (French Alps); analysis of seismic signals and their correlation with rainfalls. *Journal of Geophysical Research* **115**: F3: F03016. DOI: 10.1029/2009JF001532

Jaboyedoff M, Oppikofer T, Abellán A, Derron M-H, Loye A, Metzger R, Pedrazzini A. 2010. Use of LIDAR in landslide investigations: a review. *Natural Hazards*. DOI: 10.1007/s11069-010-9634-2

Johnson JB, Aster RC, Kyle PR. 2004. Volcanic eruptions observed with infrasound. *Geophysical Research Letters* **31**: L14604. DOI: 10.1029/2004GL020020

Lacroix P, Helmstetter A. 2011. Location of seismic signals associated with microearthquakes and rockfalls on the Séchilienne Landslide, French Alps. *Bulletin of the Seismological Society of America* **101**: 341–353.

Lajtai EZ, Gadi AM. 1989. Friction on a granite to granite interface. *Rock Mechanics and Rock Engineering* **22**: 25–49.

Lay T, Wallace T. 1995. *Modern Global Seismology*. Academic Press: New York.

Maptek. 2011. I-Site Studio Three Dimensional LiDAR Processing Software, Version 3.2. http://www.maptek.com/products/i-site/i-site_studio.html (accessed 25 May 2011).

Morrissey MM, Savage WZ, Wieczorek GF. 1999. Analysis of the 1996 Happy Isles event in Yosemite National Park. *Journal of Geophysical Research* **104**(B10): 23189–23198.

Moore JR, Sanders JW, Haught R, Cuffey KM, Glaser SD. 2007. Seismic monitoring of rockfall, Helmet Mountain, British Columbia, Canada. In *Proceedings: 1st Canada–U.S. Rock Mechanics Symposium*, Eberhardt E, Stead D, Morrison D (eds). Vancouver, British Columbia, Canada. June 2007

Moore JR, Sanders JW, Dietrich WE, Glaser SD. 2009. Influence of rock mass strength on the erosion rate of alpine cliffs. *Earth Surface Processes and Landforms* **34**: 1339–1352.

Myers SC, Rock D, Mayeda K. 2000. *Feasibility of Monitoring Rock Fall in Yosemite Valley Using Seismic Methods, LLNL report UCRL-ID-137890*. Lawrence Livermore National Laboratory: Livermore, CA.

Reyes CG, West ME. 2011. The Waveform Suite: a robust platform for manipulating waveforms in MATLAB. *Seismological Research Letters* **82**(1): 104–110.

Roth M, Blikra LH. 2009. Seismic monitoring of an unstable rock slope at Åknes, Norway. *Geophysical Research Abstracts* **11**: EGU2009-EGU3680: EGU General Assembly.

Sass O, Wollny K. 2001. Investigations regarding alpine talus slopes using ground-penetrating radar (GPR) in the Bavarian Alps, Germany. *Earth Surface Processes and Landforms* **26**: 1071–1086.

Spillman T, Maurer H, Green AG, Heinke B, Willenberg H, Husen S. 2007. Microseismic investigation of an unstable mountain slope in the Swiss Alps. *Journal of Geophysical Research* **112**: B07301. DOI. 10.1029/2006JB004723

Stock GM, Uhrhammer RL. 2010. Catastrophic rock avalanche 3600 years BP from El Capitan, Yosemite Valley, California. *Earth Surface Processes and Landforms* **35**(8): 941–951.

Stock GM, Bawden GW, Green JK, Hanson E, Downing G, Collins BD, Bond S, Leslar M. 2011. High-resolution three-dimensional imaging and analysis of rock falls in Yosemite Valley, California. *Geosphere* **7**(2): 573–581.

Uhrhammer RA. 1996. Yosemite rock fall of July 10, 1996. *Seismological Research Letters* **67**: 47–48.

Vilajosana I, Surinach E, Abellán A, Khazaradze G, Garcia D, Llosa J. 2008. Rockfall induced seismic signals: case study in Montserrat, Catalonia. *Natural Hazards and Earth System Sciences* **8**: 805–812.

Wieczorek GF. 2002. Catastrophic rockfalls and rockslides in the Sierra Nevada, USA. In *Catastrophic Landslides: Effects, Occurrence, and Mechanisms*, Evans SG, DeGraff J (eds), Geological Society of America Reviews in Engineering Geology XV. Geological Society of America: Boulder, CO; 165–190.

Wieczorek GF, Jäger S. 1996. Triggering mechanisms and depositional rates of postglacial slope-movement processes in the Yosemite Valley, California. *Geomorphology* **15**: 17–31.

Wieczorek GF, Snyder JB. 1999. *Rock Falls from Glacier Point above Camp Curry, Yosemite National Park, California, US Geological Survey Open-File Report 99–385*. US Geological Survey: Reston, VA. http://pubs.usgs.gov/of/1999/ofr-99-0385/

Wieczorek GF, Snyder JB. 2004. *Historical Rock Falls in Yosemite National Park, California, US Geological Survey Open-File Report 03–0491*. US Geological Survey: Reston, VA.

Wieczorek GF, Nishenko SP, Varnes DJ. 1995. Analysis of rock falls in the Yosemite Valley, California. In *Proceedings of the 35th US Rock Mechanics Symposium*, Reno NV, Daemen JJ, Schultz RA (eds): 85–89.

Wieczorek GF, Morrissey MM, Iovine G, Godt J. 1998. *Rock-fall Hazards in the Yosemite Valley, California, US Geological Survey Open-file Report 98–467*. US Geological Survey: Reston, VA.

Wieczorek GF, Morrissey MM, Iovine G, Godt J. 1999. *Rock-fall Potential in the Yosemite Valley, California, US Geological Survey Open-file Report 99–578*. US Geological Survey: Reston, VA.

Wieczorek GF, Snyder JB, Waitt RB, Morrissey MM, Uhrhammer RA, Harp EL, Norris RD, Bursik MI, Finewood LG. 2000. Unusual July 10, 1996 rock fall at Happy Isles, Yosemite National Park, California. *Geological Society of America Bulletin* **112**: 75–85.

Wieczorek GF, Stock GM, Reidenbach P, Snyder JB, Borchers JW, Godt JW. 2008. Investigation and hazard assessment of the 2003 and 2007 Staircase Falls rock falls, Yosemite National Park, California, USA. *Natural Hazards and Earth System Sciences* **8**: 421–432.